



Self-assembly of Ni–Fe layered double hydroxide at room temperature for oxygen evolution reaction



Seong Hyun Kim^{a,1}, Yoo Sei Park^{a,1}, Chiho Kim^a, Il Yeong Kwon^a, Jooyoung Lee^c, Hyunsoo Jin^b, Yoon Seok Lee^d, Sung Mook Choi^{c,*}, Yangdo Kim^{a,*}

^a Department of Materials Science and Engineering, Pusan National University, Busan 46241, Republic of Korea

^b Department of Mechanical Engineering, Worcester Polytechnic Institute, 100 Institute Road, Worcester, MA 01609, USA

^c Materials Center for Energy Department, Surface Technology Division, Korea Institute of Materials Science, Changwon, 642831, Republic of Korea

^d Graduate School of Natural Science and Technology, Okayama University, Okayama, 700-8530, Japan

ARTICLE INFO

Article history:

Received 22 June 2020

Received in revised form 29 September 2020

Accepted 9 October 2020

Available online 4 December 2020

Keywords:

Water electrolysis

Oxygen evolution reaction

NiFe layered double hydroxide

Room temperature synthesis

Electrocatalyst

ABSTRACT

Active and stable electrocatalysts are the key to water electrolysis for hydrogen production. This paper reports a facile direct growth method to synthesize NiFe-layered double hydroxides (LDHs) on nickel foil as an electrocatalyst for the oxygen evolution reaction. The NiFe-LDH is synthesized by a galvanic process at room temperature without any additional energy for synthesis. The synthesized NiFe-LDH is a karst landform with abundant active sites and efficient mass diffusion. The NiFe-LDH with an oxygen defect show excellent electrocatalytic performance for the OER, with a low overpotential (272 mV at 10 mA/cm²), a small Tafel slope (43 mV/dec), and superior durability. Direct growth synthesis provide excellent electrical conductivity as well as strong bonding between the catalyst layer and the substrate. In addition, this synthesis process is simple to apply in the fabrication of a large size electrode and is believed to be applicable to commercialized alkaline water electrolysis.

© 2020 The Authors. Published by Elsevier Ltd. This is an open access article under the CC BY license (<http://creativecommons.org/licenses/by/4.0/>).

1. Introduction

Electrocatalytic water splitting ($\text{H}_2\text{O} \rightarrow 1/2 \text{O}_2 + \text{H}_2$) for hydrogen generation is considered a clean and efficient hydrogen production approach. Water splitting involves the oxygen evolution reaction (OER, $4 \text{OH}^- \rightarrow 2 \text{H}_2\text{O} + 4 \text{e}^- + \text{O}_2$) and hydrogen evolution reaction (HER, $2 \text{H}_2\text{O} + 2 \text{e}^- \rightarrow 2 \text{OH}^- + \text{H}_2$) (Fabbri et al., 2014). Although the HER is a fundamental reaction for hydrogen production, the OER is more important in the overall water splitting reaction because the OER, which requires four electrons, involves more electrons than the HER, which requires two electrons (Jang et al., 2020). Hence, the OER has a higher overpotential than the HER and acts as a critical reaction that determines the overall water electrolysis efficiency (Choi et al., 2018). Therefore, a high-performance OER electrocatalyst is required to obtain a highly efficient water-splitting reaction.

Generally, precious-metal-based electrocatalysts, such as IrO₂ and RuO₂, are considered the ideal electrocatalyst for the OER owing to their high activity and superior durability (Fabbri et al., 2014; Jang et al., 2020; Choi et al., 2018). On the other hand, their

scarcity and high cost have restricted their use as an electrocatalyst. This problem can be overcome using a high-performance OER electrocatalyst based on non-precious metals. Recently, a range of OER electrocatalysts based on non-precious metals, such as Ni, Mn, Co, Cu, and Fe, have been developed (Jang et al., 2020; Choi et al., 2018; Chung et al., 2020; Kim et al., 2019; Jiang et al., 2019). These include transition metal oxides, transition metal sulfides (Park et al., 2020; Wan et al., 2019; Han et al., 2019), transition metal phosphides (Park et al., 2019; Tao et al., 2020; Xu et al., 2020), and transition metal hydroxides (Xu et al., 2018; Guo and Li, 2018; Fang et al., 2019). In particular, LDHs, a type of transition metal hydroxide, are considered an excellent electrocatalyst because of their unique layered structure with high specific surface areas and various electron distributions (Liu et al., 2017; Long et al., 2015; Yang et al., 2018; Lu et al., 2016). In addition, many studies have reported that the electrocatalyst based on the LDH structure showed high performance in the OER. Despite this, the low electrical conductivity of LDHs is a serious drawback limiting their use as an electrocatalyst for the OER (Zhang et al., 2013; Tadanaga et al., 2010). Even, polymeric binders (nafion and PTFE) are essential to fabricate electrodes using powder type electrocatalysts, but these binders also have poor electrical conductivity. The typical synthetic route of the LDH structures reported to date is a complicated process requiring more than two steps as well as a long heat treatment time at high temperatures (Yang et al., 2019; Zhong et al., 2019; Xie et al.,

* Corresponding authors.

E-mail addresses: akyzaky@kims.re.kr (S.M. Choi), yangdo@pusan.ac.kr (Y. Kim).

¹ These authors have contributed equally.

2020; Feng et al., 2020). However, in order to be applied to a commercial system, the synthesis process needs to be simplified. The complex processes lead to many variables in the development of large scale. These faults are a serious obstacle to the application of LDHs as an OER electrocatalyst to commercial water electrolysis systems. The key point to overcome is to synthesize an LDH structure simply while at the same time ensuring high electrical conductivity.

This paper proposes the self-assembly synthesis of NiFe-LDH on nickel-foil (NF) at room temperature by a galvanic process. Through the galvanic-process of NF and Fe³⁺ ions, a NiFe-LDH was grown directly on NF without any additional energy for synthesis. The NiFe-LDH was directly grown on NF without metal oxide simply by controlling the concentration of Fe(NO₃)₃. NiFe-LDH has excellent electrical conductivity between the NF and NiFe-LDH catalyst layer and a strong physical bond because it was grown directly on NF. In addition, this synthesis process is simple to apply to the fabrication of large size electrode and is considered to be applicable to commercialized alkaline water electrolysis

2. Experimental

2.1. Preparation of NiFe^x – LDH by galvanic process

NiFe^x was grown directly on NF by a galvanic corrosion reaction in an electrolyte composed of different concentrations of Fe(NO₃)₃ ($x = 0.05, 0.1, 0.15$ and 0.2 M). The Fe(III) ion act as an oxidant and corrodes the NF-substrate ($1\text{ cm} \times 2\text{ cm}$). The NF was used as a nickel ion source and current collector. The electrolyte composed of different concentrations of Fe(NO₃)₃ was prepared in amounts of 75 mL at 25 °C. Before the corrosion of NF, the surface native oxide layer of NF was removed in 6 M HCl for 30 min at 25 °C. The NF was then cleaned with acetone, ethanol, and DI water in an ultrasonic bath for 10 min. The NF was immersed completely in the electrolyte composed of Fe(NO₃)₃ for four hours at 25 °C. After the galvanic process, the NiFe^x on NF was rinsed thoroughly with DI water and dried in a convection oven at 50 °C. For comparison, commercial IrO₂ powders (Sigma Aldrich, 99.9% trace metal basis) were used as precious metal electrocatalyst. The ink solution was prepared with IrO₂ powder (20 mg), 5 wt.% nafion solution (100 ul) and ethanol (900 ul) and coated on nickel foil ($1 \times 1\text{ cm}^2$). The amount of IrO₂ was $\sim 0.5\text{ mg/cm}^2$.

2.2. Electrochemical characterization

All electrochemical analyses, including linear sweep voltammetry (LSV), cyclic voltammetry (CV), and chronopotentiometry (CP), were conducted using a potentiostat (Parstat 2273, Princeton Applied Research). The synthesized NiFe^x was carried out for the OER in a three-electrode cell with an N₂-purged 1 M KOH electrolyte at 25 °C. The reference electrode was Hg/HgO (1M KOH), and the counter electrode was a Pt-mesh, respectively. All potentials were converted to a reversible hydrogen electrode (RHE). The electrochemical surface area (ECSA) was measured by CV with different scan rates (10–160 mV/s) in the non-faradaic region in 1M KOH. The ECSA was calculated using the following equations:

$$ECSA = C_{dl}/C_s \quad (1)$$

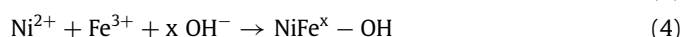
C_s is the smooth plane capacitance for a metal surface, of which value is 40 μF/cm² (McCrorry et al., 2013). The activity of the OER was examined by LSV at 5 mV/s and Tafel slope was calculated from LSV at 1 mV/s in 1M KOH. All electrochemical analysis results were iR-corrected. Electrochemical impedance spectroscopy (EIS) was conducted over the frequency range, 200 kHz to 10 Hz, with an amplitude of 10 mV at 1.58 V. The durability was measured by CP at 10 mA/cm² and 100 mA/cm² for 1200 min.

2.3. Physical property characterization

The surface morphology of NiFe^x on NF was observed by field-emission scanning electron microscopy (FESEM, CZ/MIRAI LMH, TESCAN) and a high-resolution transmission electron microscopy (TALOS F200X, Thermo Fisher Scientific). X-ray diffraction (XRD, UltimaIV, Rigaku) was performed at a scan speed of 1°/min using Cu Kα radiation. X-ray photoelectron spectroscopy (XPS) was conducted on a K-Alpha (AXIS SUPRA⁺, KRATOS Analytical) spectrometer.

3. Results and discussion

A NiFe^x ($x = 0.05, 0.1, 0.15, 0.2$ M) was grown directly on nickel foil (NF) via a galvanic corrosion reaction of Fe(III) ion and Ni at room temperature, as shown in Fig. 1. When Fe(NO₃)₃ as a precursor is dissolved in deionized water (DI), Fe³⁺ ions having higher reduction potential ($\text{Fe}^{3+} + e^- \rightarrow \text{Fe}^{2+}$; 0.77 V) than Ni ($\text{Ni}^{2+} + 2e^- \rightarrow \text{Ni}$; -0.26 V) are formed. The NF reacts with dissolved oxygen and Fe³⁺ in the solution to generate Ni²⁺ and OH⁻ ions. The chemical reaction for synthesizing NiFe^x is as follows:



The surface morphology of the synthesized NiFe^x on NF was observed by FE-SEM. The NF had a clean and smooth surface, as shown in Fig. 2a. When the concentration of Fe(NO₃)₃ was increased from 0.05 M to 0.2 M, all NiFe^x showed karst landform features, which provide abundant active sites and allow facile mass diffusion (Gao et al., 2020). In addition, as the concentration of Fe(NO₃)₃ was increased, dense NiFe^x was grown on NF, and the surface roughness increased, as shown in Fig. 2(b–e). In addition, this synthesis route is quite simple on a large scale (Fig.S1). XRD was performed to confirm the crystal structure of NiFe^x grown directly on NF, as shown in Fig. 2f. All samples showed peaks at 44.5°, 51.8°, and 76.4° 2θ, which indicated the metallic Ni (ICSD: 98-005-2265) from the Ni-foil. No recognizable XRD peaks of NiFe^x were observed in any of the samples, indicating an amorphous structure (Xie et al., 2018; Zhou et al., 2018). Further structural information of NiFe^{0.15M} was analyzed by TEM, as shown in Fig. 3a. The SAED pattern (inset of Fig. 3a) indicates the diffuse rings for the amorphous NiFe^{0.15M}. In addition, there are no recognizable lattice fringes can be observed from HR-TEM images (Fig. 3b). These results were consistent with the analysis in XRD results. Elemental mapping results of NiFe^{0.15M} showed a uniform distribution of Ni, Fe and O, as shown in Fig. 3c.

Since synthesis at low temperature results in low crystallinity, the synthesized NiFe^x at room temperature has low crystallinity (Gan et al., 2019). Raman spectroscopy was conducted to examine the structure of NiFe^x, as shown in fig.S2. All samples showed a broad band at 530 cm⁻¹, suggesting that NiFe-LDH was defective or disordered (Lu et al., 2014; Louie and Bell, 2013). On the other hand, NiFe^{0.2M} showed an additional shoulder band at $\sim 660\text{ cm}^{-1}$, indicating Fe–O in iron oxide (Muniz-Miranda et al., 2020). These oxides originated from the harsh oxidation conditions due to the high concentration of Fe(NO₃)₃.

XPS was performed to confirm the elemental structure of the synthesized NiFe^x, as shown in Fig. 4. The high-resolution spectra of the Ni 2p region revealed two peaks, 2p_{3/2} ($\sim 855\text{ eV}$) and 2p_{1/2} ($\sim 873\text{ eV}$), due to spin-orbit coupling. The Ni of NiFe^{0.05M} in Ni 2p_{3/2} showed three oxidation states: Ni⁰ ($\sim 853\text{ eV}$), Ni²⁺ ($\sim 854.9\text{ eV}$), and Ni³⁺ ($\sim 855.3\text{ eV}$), as shown in fig.S4. The NiFe^{0.05M} was grown at a low Fe(NO₃)₃ concentration, so NiFe^{0.05} was not fully

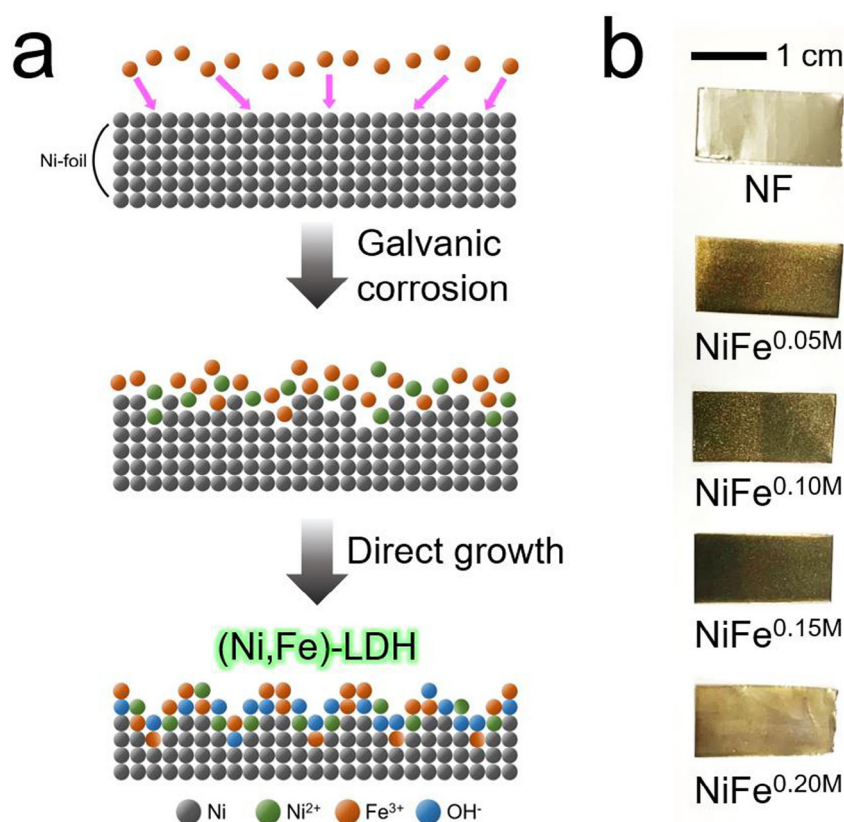


Fig. 1. (a) Schematic diagram of NiFe-LDH on Ni-foil (NF) by a galvanic corrosion reaction. (b) photograph of NiFe^x (x = 0.05, 0.1, 0.15 and 0.2 M) on NF.

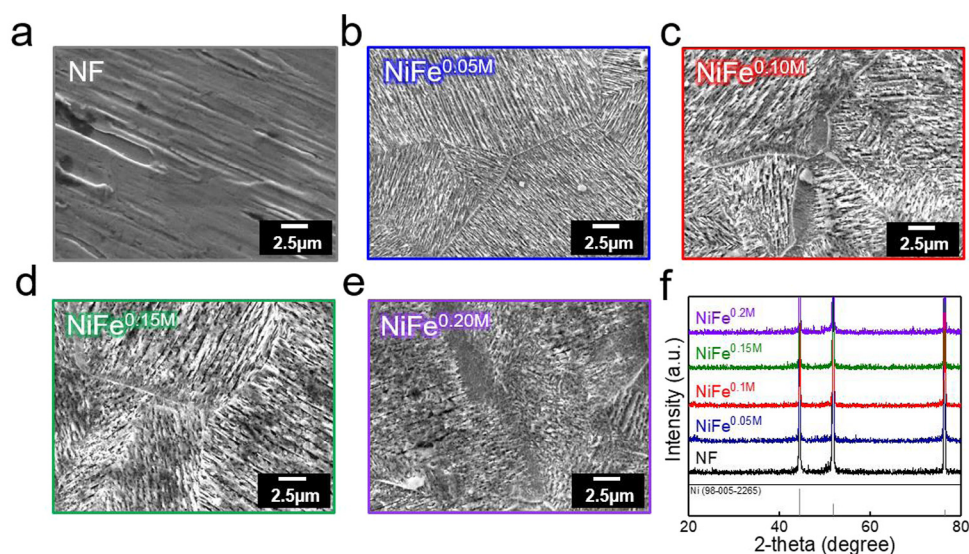


Fig. 2. (a–e) FE-SEM images of NF and the karst landform-featured surface of NiFe^x on NF (x = 0.05, 0.1, 0.15 and 0.2 M). (f) XRD pattern of NiFe^x on NF.

grown on the surface of the NF. Therefore, the Ni of NF, which was Ni⁰. Ni³⁺ in NiFe^{0.05M} was observed on the Ni due to the low concentration of Ni²⁺ near the NF surface. Because Fe³⁺ is a strong oxidant that reduces to Fe²⁺, Fe³⁺ oxidizes NF to form Ni²⁺ and simultaneously oxidizes the Ni²⁺ generated from NF to Ni³⁺. When the concentration of Fe(NO₃)₃ was increased, the observed oxidation state of Ni³⁺ shifted to Ni²⁺. The corrosion of NF proceeded rapidly when the Fe(NO₃)₃ concentration was increased. Therefore, the peak intensity of Ni²⁺ increases because the rate at which Ni²⁺ is produced is faster than the rate at which Ni²⁺ is oxidized to Ni³⁺. The high-resolution spectra of the Fe

2p region showed two peaks, 2p_{3/2} (~712 eV) and 2p_{1/2} (~722 eV). Although the concentration of Fe(NO₃)₃ increased from 0.05 to 0.15 M, the oxidation state of Fe was only +3, as shown in Fig. 4b. On the other hand, the peak position of Fe 2p_{3/2} and 2p_{1/2} shifted in the positive direction, which is related to the negative shift of Ni 2p_{3/2} and Ni 2p_{1/2}. The positive shift of Fe 2p indicates the accumulation of electrons around the Ni site, and the negative shift of Ni 2p indicates a decrease in the number of electrons at the Fe site (Jiao et al., 2019). These changes in electron accumulation changed the electron distribution, which altered the local electronic structure of the metal site. When the

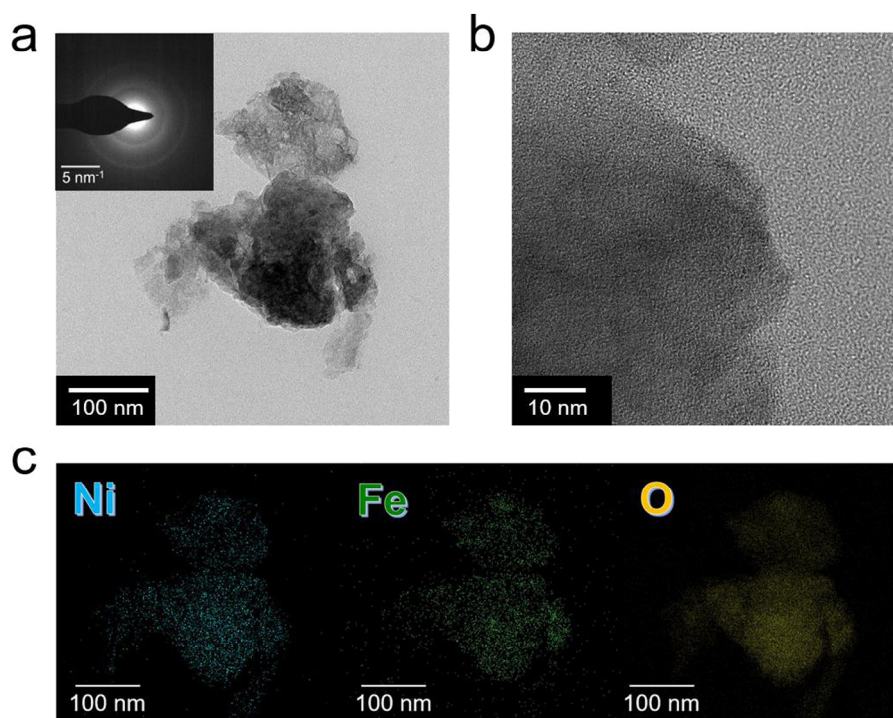


Fig. 3. (a) TEM images of NiFe^{0.15M} with SAED patterns. (b) HR-TEM images of NiFe^{0.15M}. (c) TEM-EDS mapping of Ni (cyan), Fe (green) and O (yellow).

concentration of Fe (NO₃)₃ was 0.2 M, Fe³⁺ and Fe²⁺ coexisted with an increase of the peak intensity of Fe²⁺, as shown in fig.S5. In particular, the difference in binding energy between 2p_{3/2} (710.1 eV) and 2p_{1/2} (723.5 eV) in NiFe^{0.2M} was ~13.5 eV, which was different from NiFe^x (x = 0.05, 0.1 and 0.15 M) synthesized at other Fe(NO₃)₃ concentrations. In previous studies, the binding energy difference between Fe 2p_{3/2} and Fe 2p_{1/2} was related to the oxidation state of Fe. The binding energy difference of NiFe^x (x = 0.05, 0.1 and 0.15 M) was measured approximately 12 eV and binding energy difference of NiFe^{0.2M} was approximately 12.4 eV. This binding energy difference indicate tri-valent oxidation state (Fe³⁺) (Li et al., 2017; Wu et al., 2011). However, the Fe in NiFe^{0.2M} was deconvoluted by Fe²⁺ and Fe³⁺, as shown in fig.S5. When combined with the XPS analysis of O 1s, NiFe^x (x = 0.05, 0.1 and 0.15 M) is considered as NiFe-LDH, and NiFe^{0.2M} is considered as a mixture of NiFe-LDH and NiFe-oxide. These results indicated that high concentrations of Fe(NO₃)₃ produced a harsh oxidizing condition; hence, NiFe-oxide, rather than NiFe-LDH, was synthesized. The O 1s spectra of all NiFe^x were deconvoluted to hydroxyl groups (O_{OH}), oxygen vacancies (O_V), and chemisorbed water (O_W) (Xu et al., 2018). In addition, the O_L observed in the oxide was present in NiFe^{0.2M} because of the harsh oxidation conditions. The O_V indicates a defect site with low oxygen coordination, which decrease the barrier for the adsorption of OH⁻ and promotes OER. In particular, NiFe^{0.1M} and NiFe^{0.15M} had a similar area of O_{OH} (~50%), but O_V showed a clear difference. NiFe^{0.15M} has a higher oxygen defect density than NiFe^{0.1M} (~30%: ~21%).

Linear scan voltammetry (LSV) was performed on N₂-purged 1M KOH to observe the OER performance of the synthesized NiFe^x (x = 0.05, 0.1, 0.15, and 0.2 M), as shown in Fig. 5a. Pure NF showed poor OER activity, which was an overpotential of 371 mV at 10 mA/cm². To compare with the precious metal electrocatalyst, IrO₂ was coated on NF, and an OER test was performed under the same conditions, which was an overpotential of 347 mV at 10 mA/cm², as shown in Fig.S6. Fig. 5b shows the overpotential of NiFe^x (x = 0.05, 0.1, 0.15, and 0.2 M). The NiFe^{0.05M} has low catalytic activity for the OER because of the low coverage of the

catalyst layer on the surface, and NiFe^{0.2M} has low OER performance because of the oxide formed on the surface. In particular, NiFe^{0.15M} had an extremely low overpotential of 272 mV at 10 mA/cm² because of the abundant oxygen defects. Table S1 lists the performance of OER catalysts deposited on flat substrates, such as metal foil. The Tafel slope is an important factor showing the mechanism in the OER. The Tafel slope of the synthesized NiFe^x was calculated from LSV, and the slope of all synthesized NiFe^x was approximately 40 mV/dec, as shown in Fig. 5c. In the OER, there were three theoretical Tafel slopes: 40, 60, and 120 mV/dec (Han et al., 2017; Zhou et al., 2017). The Tafel slope of 40 mV/dec indicated that the second electron transfer was the rate-determining step (rds), and the Tafel slope of 60 mV/dec indicated that an OH⁻ intermediate coverage step after the first electron-transfer step was the rds (Choi et al., 2018). A Tafel slope of 120 mV/dec means a single electron transfer step without a pre-equilibrium step. Therefore, the second electron transfer reaction was the rds of all synthesized NiFe^x. To measure the electrochemically active surface area (ECSA) of the synthesized NiFe^x, the double-layer capacitance (C_{dl}) was calculated in the non-faradaic region by cyclic voltammetry, as shown in fig.S7. The measured values of C_{dl} showed the same trend, as obtained by LSV, as shown in Fig. 5d. The NiFe^{0.15M} had a higher ECSA (61.75 cm_{ECSA}²) than NiFe^{0.05M} (34.75 cm_{ECSA}²), NiFe^{0.1M} (46.00 cm_{ECSA}²), and NiFe^{0.2M} (32.25 cm_{ECSA}²). The large ECSA contributed partially to the fastest catalytic kinetics. To calculate the activity of the OER per ECSA, the LSV was normalized with ECSA (Fig. S8). Similar to the above result, NiFe^{0.15M} showed the best OER performance per active electrochemical site. The exchange current density (i₀) was calculated from the Tafel slope to verify the intrinsic kinetic properties of the synthesized NiFe^x (Suen et al., 2017). The i₀ of the synthesized NiFe^x (x = 0.05, 0.1, 0.15, and 0.2M) was approximately 0.0004, 0.0009, 0.005, and 0.0008 μA/cm², respectively. These results confirmed that the NiFe^{0.15M} showed the optimal intrinsic activity for the OER, as shown in fig.S9. To obtain the charge transfer resistance (R_{ct}), electrochemical impedance spectroscopy (EIS) was conducted at 1.58 V vs. RHE. Similar to

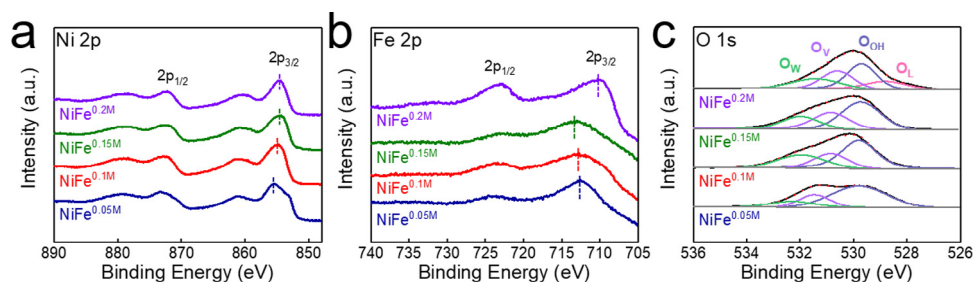


Fig. 4. (a) High-resolution XPS spectra of Ni 2p, (b) XPS spectra of Fe 2p, (c) XPS spectra of O 1s. The dot lines in Ni 2p and Fe 2p indicate the 2p_{3/2} peak. The O_L, O_{OH}, O_V, and O_W in O 1s indicate lattice oxygen, hydroxyl species, oxygen vacancy, and chemisorbed water.

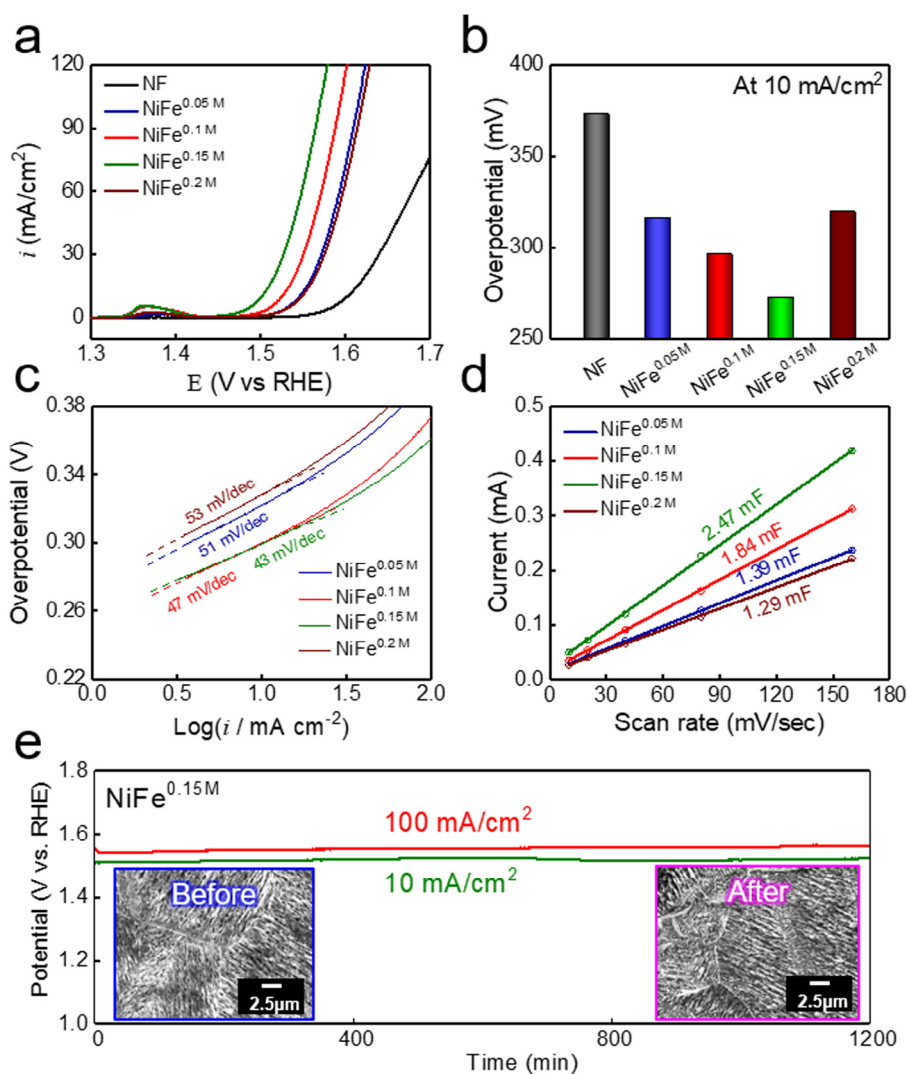


Fig. 5. OER on NiFe^x (*x* = 0.05, 0.1, 0.15 and 0.2 M) on Ni-foil. (a) LSV curves of NF and NiFe^x recorded at a scan rate of 5 mV/s in N₂-saturated 1M KOH. (b) Comparison of the overpotential for OER at 10 mA/cm². (c) Tafel slope of NiFe^x. (d) double layer capacitance (C_{dl}) of NiFe^x. (e) Durability test of NiFe^{0.15M} at 100 mA/cm².

the results of the previous electrochemical analysis results, the NiFe^{0.15M} had the lowest *R*_{ct} value than the other NiFe^x (Fig. S10). Constant current tests were conducted to confirm the durability. The NiFe^{0.15M}, which was the best OER electrocatalyst, was tested, and a change in overpotential was observed while applying a current of 10 and 100 mA/cm² for 1200 min. In addition, almost no sign of decay was observed, as shown in Fig. 5e. The surface morphology of NiFe^{0.15M} was not changed, which meant that physical desorption was minimized due to the strong bonding

of the catalyst layer (NiFe^{0.15M}) and substrate (NF). In addition, to confirm the change of chemical state of NiFe^{0.15M} after the durability test, we conducted XPS analysis, as shown in fig.S11. The chemical states of Ni after the durability test were observed as 2+ and 3+. In addition, the chemical state of Fe was observed as 3+. No other change of component was observed in Ni and Fe. These results indicate that NiFe^{0.15M} has good chemical durability.

4. Conclusion

NiFe-LDH was grown directly on nickel-foil by a galvanic corrosion reaction and showed excellent OER performance. This synthesis process was facile and did not require external energy for synthesis. The NiFe^{0.15M} synthesized in 0.15 M Fe(NO₃)₃ exhibited the highest OER activity with an overpotential of 272 mV at 10 mA/cm² and a low Tafel slope of 43 mV/dec due to the abundant oxygen defects, which were much higher than the IrO₂ electrocatalyst. The direct growth of the NiFe electrocatalyst on nickel foil prevented physical detachment of the catalyst layer through strong bonding between the catalyst layer and substrate and provided excellent electrical conductivity by lowering the ohmic contact resistance. This unique synthesis process by the galvanic corrosion reaction can be applied easily to the fabrication of large electrodes and is applicable to commercialized alkaline water electrolysis.

CRedit authorship contribution statement

Seong Hyun Kim: Writing – original draft, Maintained the lead position in research, Synthesized the electrocatalysts, Evaluated their electrochemical properties. **Yoo Sei Park:** Writing – original draft, Maintained the lead position in research. **Chiho Kim:** Synthesized the electrocatalysts, Evaluated their electrochemical properties. **Il Yeong Kwon:** Assisted the physical characterizations. **Jooyoung Lee:** Assisted the physical characterizations. **Hyunsoo Jin:** Assisted the physical characterizations. **Yoon Seok Lee:** Synthesized the electrocatalysts, Evaluated their electrochemical properties. **Sung Mook Choi:** Supervision, Improved the concept of research, Setting up experiments. **Yangdo Kim:** Supervision, Improved the concept of research, Setting up experiments.

Declaration of competing interest

The authors declare that they have no known competing financial interests or personal relationships that could have appeared to influence the work reported in this paper.

Acknowledgment

This research was supported by Basic Science Research Program through the National Research Foundation of Korea (NRF) funded by the Ministry of Education (No. NRF-2016R1D1A3B04935101).

Appendix A. Supplementary data

Supplementary material related to this article can be found online at <https://doi.org/10.1016/j.egy.2020.10.007>.

References

- Choi, W.-S., Jang, M.J., Park, Y.S., Lee, K.H., Lee, J.Y., Seo, M.-H., Choi, S.M., 2018. Three-dimensional honeycomb-like Cu_{0.8}Co_{2.19}O₄ nanosheet arrays supported by Ni foam and their high efficiency as oxygen evolution electrodes. *ACS Appl. Mater. Interfaces* 10, 38663–38668.
- Chung, D.Y., Lopes, P.P., Farinazzo Bergamo Dias Martins, P., He, H., Kawaguchi, T., Zapol, P., You, H., Tripkovic, D., Strmcnik, D., Zhu, Y., Seifert, S., Lee, S., Stamenkovic, V.R., Markovic, N.M., 2020. Dynamic stability of active sites in hydr(oxy)oxides for the oxygen evolution reaction. *Nat. Energy* 5, 222–230.
- Fabbri, E., Haberer, A., Waltar, K., Kötz, R., Schmidt, T.J., 2014. Developments and perspectives of oxide-based catalysts for the oxygen evolution reaction. *Catal. Sci. Technol.* 4, 3800–3821.
- Fang, G., Cai, J., Huang, Z., Zhang, C., 2019. One-step electrodeposition of cerium-doped nickel hydroxide nanosheets for effective oxygen generation. *RSC Adv.* 9, 17891–17896.
- Feng, L., Du, Y., Huang, J., Cao, L., Feng, L., Feng, Y., Liu, Q., Yang, D., Kajiyoshi, K., 2020. Nanoporous NiAl-LDH nanosheet arrays with optimized Ni active sites for efficient electrocatalytic alkaline water splitting. *Sustain. Energy Fuels*.

- Gan, Q., Cheng, X., Chen, J., Wang, D., Wang, B., Tian, J., Isimjan, T.T., Yang, X., 2019. Temperature effect on crystallinity and chemical states of nickel hydroxide as alternative superior catalyst for urea electrooxidation. *Electrochim. Acta* 301, 47–54.
- Gao, X., Chen, Y., Sun, T., Huang, J., Zhang, W., Wang, Q., Cao, R., 2020. Karst landform-featured monolithic electrode for water electrolysis in neutral media. *Energy Environ. Sci.* 13, 174–182.
- Guo, C.X., Li, C.M., 2018. Room temperature-formed iron-doped nickel hydroxide on nickel foam as a 3D electrode for low polarized and high-current-density oxygen evolution. *Chem. Commun.* 54, 3262–3265.
- Han, L., Dong, C., Zhang, C., Gao, Y., Zhang, J., Gao, H., Wang, Y., Zhang, Z., 2017. Dealloying-directed synthesis of efficient mesoporous CoFe-based catalysts towards the oxygen evolution reaction and overall water splitting. *Nanoscale* 9, 16467–16475.
- Han, C., Li, W., Shu, C., Guo, H., Liu, H., Dou, S., Wang, J., 2019. Catalytic activity boosting of nickel sulfide toward oxygen evolution reaction via confined overdoping engineering. *ACS Appl. Energy Mater.* 2, 5363–5372.
- Jang, M.J., Yang, J., Lee, J., Park, Y.S., Jeong, J., Park, S.M., Jeong, J.-Y., Yin, Y., Seo, M.-H., Choi, S.M., Lee, K.H., 2020. Superior performance and stability of anion exchange membrane water electrolysis: pH-controlled copper cobalt oxide nanoparticles for the oxygen evolution reaction. *J. Mater. Chem. A* 8, 4290–4299.
- Jiang, H., He, Q., Li, X., Su, X., Zhang, Y., Chen, S., Zhang, S., Zhang, G., Jiang, J., Luo, Y., Ajayan, P.M., Song, L., 2019. Tracking structural self-reconstruction and identifying true active sites toward cobalt oxychloride precatalyst of oxygen evolution reaction. *Adv. Mater.* 31, 1805127.
- Jiao, S., Yao, Z., Li, M., Mu, C., Liang, H., Zeng, Y.-J., Huang, H., 2019. Accelerating oxygen evolution electrocatalysis of two-dimensional NiFe layered double hydroxide nanosheets via space-confined amorphization. *Nanoscale* 11, 18894–18899.
- Kim, B.-J., Fabbri, E., Abbott, D.F., Cheng, X., Clark, A.H., Nachtegaal, M., Borlaf, M., Castelli, I.E., Graule, T., Schmidt, T.J., 2019. Functional role of Fe-doping in Co-based perovskite oxide catalysts for oxygen evolution reaction. *J. Am. Chem. Soc.* 141, 5231–5240.
- Li, L., Bi, H., Gai, S., He, F., Gao, P., Dai, Y., Zhang, X., Yang, D., Zhang, M., Yang, P., 2017. Uniformly dispersed ZnFe₂O₄ nanoparticles on nitrogen-modified graphene for high-performance supercapacitor as electrode. *Sci. Rep.* 7, 43116.
- Liu, H., Wang, Y., Lu, X., Hu, Y., Zhu, G., Chen, R., Ma, L., Zhu, H., Tie, Z., Liu, J., Jin, Z., 2017. The effects of Al substitution and partial dissolution on ultrathin NiFe layered double hydroxide nanosheets for oxygen evolution reaction in alkaline solution. *Nano Energy* 35, 350–357.
- Long, X., Xiao, S., Wang, Z., Zheng, X., Yang, S., 2015. Co intake mediated formation of ultrathin nanosheets of transition metal LDH—an advanced electrocatalyst for oxygen evolution reaction. *Chem. Commun.* 51, 1120–1123.
- Louie, M.W., Bell, A.T., 2013. An investigation of thin-film Ni-Fe oxide catalysts for the electrochemical evolution of oxygen. *J. Am. Chem. Soc.* 135, 12329–12337.
- Lu, Z., Qian, L., Tian, Y., Li, Y., Sun, X., Duan, X., 2016. Ternary NiFeMn layered double hydroxides as highly-efficient oxygen evolution catalysts. *Chem. Commun.* 52, 908–911.
- Lu, Z., Xu, W., Zhu, W., Yang, Q., Lei, X., Liu, J., Li, Y., Sun, X., Duan, X., 2014. Three-dimensional NiFe layered double hydroxide film for high-efficiency oxygen evolution reaction. *Chem. Commun.* 50, 6479–6482.
- McCrorry, C.C.L., Jung, S., Peters, J.C., Jaramillo, T.F., 2013. Benchmarking heterogeneous electrocatalysts for the oxygen evolution reaction. *J. Am. Chem. Soc.* 135, 16977–16987.
- Muniz-Miranda, M., Muniz-Miranda, F., Giorgetti, E., 2020. Spectroscopic and microscopic analyses of Fe₃O₄/Au nanoparticles obtained by laser ablation in water. *Nanomaterials* 10.
- Park, Y.S., Choi, W.-S., Jang, M.J., Lee, J.H., Park, S., Jin, H., Seo, M.H., Lee, K.-H., Yin, Y., Kim, Y., Yang, J., Choi, S.M., 2019. Three-dimensional dendritic Cu-Co-P electrode by one-step electrodeposition on a hydrogen bubble template for hydrogen evolution reaction. *ACS Sustain. Chem. Eng.* 7, 10734–10741.
- Park, Y.S., Lee, J.H., Jang, M.J., Jeong, J., Park, S.M., Choi, W.-S., Kim, Y., Yang, J., Choi, S.M., 2020. Co₃S₄ nanosheets on Ni foam via electrodeposition with sulfurization as highly active electrocatalysts for anion exchange membrane electrolyzer. *Int. J. Hydrogen Energy* 45, 36–45.
- Suen, N.-T., Hung, S.-F., Quan, Q., Zhang, N., Xu, Y.-J., Chen, H.M., 2017. Electrocatalysis for the oxygen evolution reaction: recent development and future perspectives. *Chem. Soc. Rev.* 46, 337–365.
- Tadanaga, K., Furukawa, Y., Hayashi, A., Tatsumisago, M., 2010. Direct ethanol fuel cell using hydrotalcite clay as a hydroxide ion conductive electrolyte. *Adv. Mater.* 22, 4401–4404.
- Tao, X., Luo, S., Tian, C., Qing, Y., Lu, X., Yan, N., Wu, Y., 2020. Ni@Ni₂P Encapsulation in interconnected N-doped carbonized cellulose nanofibril network for efficient oxygen evolution reaction. *ACS Sustain. Chem. Eng.* 8, 1859–1867.

- Wan, K., Luo, J., Zhou, C., Zhang, T., Arbiol, J., Lu, X., Mao, B.-W., Zhang, X., Fransaer, J., 2019. Hierarchical porous Ni_3S_4 with enriched high-valence Ni sites as a robust electrocatalyst for efficient oxygen evolution reaction. *Adv. Funct. Mater.* 29, 1900315.
- Wu, P., Du, N., Zhang, H., Yu, J., Yang, D., 2011. Carbon nanocapsules as nanoreactors for controllable synthesis of encapsulated iron and iron oxides: Magnetic properties and reversible lithium storage. *J. Phys. Chem. C* 115, 3612–3620.
- Xie, X., Cao, C., Wei, W., Zhou, S., Wu, X.-T., Zhu, Q.-L., 2020. Ligand-assisted capping growth of self-supporting ultrathin FeNi-LDH nanosheet arrays with atomically dispersed chromium atoms for efficient electrocatalytic water oxidation. *Nanoscale* 12, 5817–5823.
- Xie, J., Qu, H., Lei, F., Peng, X., Liu, W., Gao, L., Hao, P., Cui, G., Tang, B., 2018. Partially amorphous nickel-iron layered double hydroxide nanosheet arrays for robust bifunctional electrocatalysis. *J. Mater. Chem. A* 6, 16121–16129.
- Xu, W., Lyu, F., Bai, Y., Gao, A., Feng, J., Cai, Z., Yin, Y., 2018. Porous cobalt oxide nanoplates enriched with oxygen vacancies for oxygen evolution reaction. *Nano Energy* 43, 110–116.
- Xu, B., Yang, X., Fang, Q., Du, L., Fu, Y., Sun, Y., Liu, Q., Lin, Q., Li, C., 2020. Anion-cation dual doping: An effective electronic modulation strategy of Ni₂P for high-performance oxygen evolution. *J. Energy Chem.* 48, 116–121.
- Yang, Y., Dang, L., Shearer, M.J., Sheng, H., Li, W., Chen, J., Xiao, P., Zhang, Y., Hamers, R.J., Jin, S., 2018. Highly active trimetallic NiFeCr layered double hydroxide electrocatalysts for oxygen evolution reaction. *Adv. Energy Mater.* 8, 1703189.
- Yang, R., Zhou, Y., Xing, Y., Li, D., Jiang, D., Chen, M., Shi, W., Yuan, S., 2019. Synergistic coupling of CoFe-LDH arrays with NiFe-LDH nanosheet for highly efficient overall water splitting in alkaline media. *Appl. Catal. B* 253, 131–139.
- Zhang, P., Sago, S., Yamaguchi, T., Anilkumar, G.M., 2013. Mg-Al layered double hydroxides containing glycine betaine as low humidity-dependent anion conducting electrolyte material for solid state alkaline fuel cell (SAFC). *J. Power Sources* 230, 225–229.
- Zhong, H., Liu, T., Zhang, S., Li, D., Tang, P., Alonso-Vante, N., Feng, Y., 2019. Template-free synthesis of three-dimensional NiFe-LDH hollow microsphere with enhanced OER performance in alkaline media. *J. Energy Chem.* 33, 130–137.
- Zhou, Q., Li, T.-T., Qian, J., Xu, W., Hu, Y., Zheng, Y.-Q., 2018. CuO nanorod arrays shelled with amorphous NiFe layered double hydroxide film for enhanced electrocatalytic water oxidation activity. *ACS Appl. Energy Mater.* 1, 1364–1373.
- Zhou, M., Weng, Q., Zhang, X., Wang, X., Xue, Y., Zeng, X., Bando, Y., Golberg, D., 2017. In situ electrochemical formation of core-shell nickel-iron disulfide and oxyhydroxide heterostructured catalysts for a stable oxygen evolution reaction and the associated mechanisms. *J. Mater. Chem. A* 5, 4335–4342.